Energy Storage Materials 33 (2020) 139–146

Contents lists available at ScienceDirect

Energy Storage Materials

journal homepage: www.elsevier.com/locate/ensm

Tuning bifunctional interface for advanced sulfide-based all-solid-state batteries

Feipeng Zhao [a], Yang Zhao [a], Jian Wang [b], Qian Sun [a], Keegan Adair [a], Shumin Zhang [a], Jing Luo [a], Junjie Li [a], Weihan Li [a], Yipeng Sun [a], Xiaona Li [a], Jianwen Liang [a], Changhong Wang [a], Ruying Li [a], Huan Huang [c], Li Zhang [d], Shangqian Zhao [d], Shigang Lu [d], Xueliang Sun [a,*]

[a] Department of Mechanical and Materials Engineering, University of Western Ontario, London, Ontario, N6A 5B9, Canada
[b] Canadian Light Source Inc, University of Saskatchewan, Saskatoon, Saskatchewan, S7N 2V3, Canada
[c] Glabat Solid-State Battery Inc, 700 Collip Circle, London, Ontario, N6G 4X8, Canada
[d] China Automotive Battery Research Institute Co., Ltd, 5th Floor, No. 43, Mining Building, North Sanhuan Middle Road, Haidian District, Beijing, P.C. 100088, China

ARTICLE INFO

Keywords:
All-solid-state lithium-ion batteries (ASSLIBs)
Cathode interfaces
Interfacial manipulations
Sulfide electrolytes
Atomic layer depositions (ALD)

ABSTRACT

The development of high-performance sulfide electrolyte-based all-solid-state lithium-ion batteries (ASSLIBs) has been inhibited by problematic ionic transport and side reactions at the cathode interface, and their success is dependent on the functionalized interface upon charging and discharging. Despite recent progresses, it has proven challenging to design a favorable interface that can suppress the side reactions and enable smooth motion of Li^+ ions. Herein, a favorable Zr-based cathode interface is elaborately manipulated by the atomic layer deposition (ALD) for sulfide-based ASSLIBs. Flexile control over the Li sub-cycle during the preparation process is demonstrated to be crucial for achieving a robust cathode interface with a desirable Li^+ ionic conductivity. The ASSLIBs equipped with this functional interface exhibit excellent cycling stability and rate capability at room temperature (RT). Various electrochemical and spectroscopic characterizations reveal that the ionic conductive interface can significantly limit side reactions and induce a low polarization of the (de)intercalation toward cathode materials. The interfacial manipulation regarding ionic conductivity and structure realized by ALD provides a new strategy to achieve high-performance ASSLIBs.

1. Introduction

Sulfide electrolyte-based all-solid-state Li-ion batteries (ASSLIBs) have attracted significant interest due to their intrinsic safety and high-energy-density compared to the conventional Li-ion batteries (LIBs) using organic liquid electrolytes [1–3]. However, issues associated with the interfacial compatibility between sulfide-electrolytes and the anode/cathode have inhibited their commercialization [4–6]. Utilizations of Li alloys (Li–In, Li–Al, Li–Sn, etc) or chemically/electrochemically pretreated Li metal anodes can effectively alleviate the anode interfacial problems [7–9]. In contrast, limited strategies have been demonstrated to stabilize the cathode interface in sulfide electrolyte-based ASSLIBs. The thermodynamic incompatibility of the cathode/sulfide electrolytes results in unfavorable side reactions and hampered Li^+ ion conductivity [10–12]. Development of functional coating layers on cathode particles is the most commonly used method to improve the stability of the cathode/sulfide electrolytes interface [13,14].

The Zirconium (Zr)-based coating layer (ZrO_x or $LiZrO_x$) is one of the most promising cathode coating materials for ASSLIBs [10,13]. Both simulation and experimental results have shown that improved electrochemical performance can be achieved by coating the Zr-based interface layers on cathode materials [10,15–17]. Very recently, Samsung employed one Li_2O–ZrO_2 coating to endow a pouch cell-type sulfide electrolyte-based ASSLIB with an impressive cycling performance of 1000 cycles at 60 °C [16]. Compared with the common-used $LiNO_x$ or $LiTaO_x$ coating layers for sulfide-based ASSLIBs [10,13], the Zr-based coating is predicted to improve the rate performance, because the derived Zr-based interface is capable of optimizing the electrical band structure to achieve an appropriate electronic conductivity [18]. In addition, the Zr-based rock-salt structure layer coated on the Li and Mn-rich (LMR) cathodes was also proved to suppress the deleterious phase transformation of the cathode materials in the liquid

* Corresponding author.
E-mail address: xsun9@uwo.ca (X. Sun).

https://doi.org/10.1016/j.ensm.2020.06.013
Received 7 April 2020; Received in revised form 18 May 2020; Accepted 8 June 2020
Available online 16 August 2020

electrolyte-based Li-ion batteries [19]. Last but not least, the Zr element is much more abundant in the earth's crust compared with Nb or Ta, which can leading to a lower fabrication cost for practical applications [20].

Li-containing coatings are important to provide required interfacial ionic conductivity (σ) for sulfide-based ASSLIBs [13]. By revisiting the reported Li-containing Zr-based coating ($LiZrO_x$), it is found that most of these coatings were developed via wet chemical approaches, and high temperature (HT, ≥ 650 °C) post-annealing was commonly employed to remove the organic solvent and achieve crystallized coatings [15,16,21–27]. Nevertheless, the involved high-temperature process was reported to have the potential to cause degradation or phase change of the cathode materials, particularly for the interface-sensitive solid-state systems [13]. It is noted that Samsung's Li_2O–ZrO_2 cathode coating is among few wet chemical methods that employ low-temperature (LT) processes (350 or 300 °C) [15,16], but contributes to one of the best electrochemical performance in the field of ASSLIBs [11]. The obtained amorphous Li-containing Zr-based coating from LT process was verified to possess a sufficient σ and intact morphology to realize the excellent performance [13,16,27]. Therefore, development of LT or solvent-free routes is necessary to avoid the negative effects brought about by the HT process.

Atomic layer deposition (ALD) is an advanced film fabricating technique, capable of tuning the interface property with atomic-level thickness control at relatively low temperature (<400 °C) [28]. Compared with the conventional wet chemical method, the ALD method can not only show the ability of developing Li-containing transition metal oxides coating with uniform and conformal features, but also completely avoid the negative effects of using solvents and HT processes [29]. ALD-$LiNbO_x$ [30,31] and ALD-$LiPO_x$ [32] have been reported as effective cathode coatings to improve the interfacial compatibility between cathode materials and $Li_{10}GeP_2S_{12}$ (LGPS) sulfide electrolytes. However, the detailed Li^+ ion conducing effect derived from the ALD process on the electrochemical performance of sulfide-based ASSLIBs is still unknown, but undoubtedly plays a very important role.

Herein, for the first time, we choose Zr as the transition metal and develop a new lithium zirconium oxide (LZO) in alleviating the incompatible interface between $LiCoO_2$ (LCO) cathodes and Li_6PS_5Cl (LPSCl) sulfide electrolytes. The Zr-based film with and without Li incorporation obtained by ALD (abbreviated as ALD-LZO and ALD-ZrO_x, respectively) shows significant differences on the structure of the film, as well as the electrochemical performance of the ASSLIBs. The tunable σ of LZO layer manipulated by the preparation process is crucial for the delivered performance of the ASSLIBs. Furthermore, the working mechanism of ALD-LZO coating to guarantee the interfacial stability is disclosed via multiple advanced chemical/electrochemical characterizations.

2. Material and methods

2.1. Synthesis of ALD-LZO and ALD-ZrO_x films

N-doped carbon nanotubes (CNTs, prepared by previously reported chemical vapor deposition method [33]), $LiCoO_2$ (LCO, Sigma Aldrich, 99.8%), and glass slides were used as the substrates for established purposes. Tetrakis(dimethylamido) zirconium (IV) (TDMAZ, STREM CHEMICALS, INC. 99%), lithium *tert*-butoxide (LiO^tBu, STREM CHEMICALS, INC. > 98%), and deionized H_2O were used as the precursors. TDMAZ and LiO^tBu were kept at 75 °C and 170 °C respectively with heating jackets to provide vapor, while H_2O was kept at room temperature to provide vapor. For the ALD-LZO preparation, two separated sub-cycles (LiO_x and ZrO_x) are required as shown in Fig. S1 in the supplementary material. One single LiO_x sub-cycle process: (1) a 1 s pulse of LiO^tBu; (2) a 2 s extended exposure of LiO^tBu to the substrate; (3) purging of residual LiO^tBu with 12 s; (4) a 1.0 s pulse of H_2O; (5) a 1.0 s extended exposure of water vapor to the substrate; (6) a 20 s purge of residual H_2O. One single ZrO_x sub-cycle process: (1) a 1 s pulse of TDMAZ; (2) a 2 s extended exposure of TDMAZ to the substrate; (3) purging of residual TDMAZ with 12 s; (4) a 1.0 s pulse of H_2O; (5) a 1.0 s extended exposure of H_2O vapor to the substrate; (6) a 18 s purge of residual H_2O. One full cycle of ALD-LZO process includes one LiO_x sub-cycle and 4 ZrO_x sub-cycles. The deposition temperature was optimized as 270 °C based on the obtained ionic conductivity (230 °C and 300 °C were both tried). N_2 was used as the carrier gas and the ALD reactor was sustained at a high vacuum of 0.2 Torr with a continuously working pump. Just performing the sub-cycle of ZrO_x to prepare ALD-ZrO_x films on designate substrates.

2.2. Synthesis of Li_6PS_5Cl (LPSCl) SSEs

Li_2S (Alfa Aesar, 99.9%), P_2S_5 (Sigma Aldrich, >99%), and LiCl (Sigma Aldrich, 99.9%, anhydrous) or LiCl (Sigma Aldrich, > 99.98%, anhydrous) were used as the starting materials. As the previously reported solid-state reaction method [34], stoichiometric starting materials were weighted and sealed in a zirconia ball-milling pot with a weight ratio of 1:40 (starting materials: zirconia balls) in an Ar-filled glovebox (H_2O < 0.1 ppm, O_2 < 0.1 ppm). The mixture was mechanically milled by using a planetary ball milling apparatus at 510 rpm for 13 h. Then, the ball-milled product was pressed into pellets, sealed in quartz tubes for annealing (550 °C for 8 h) in a muffle furnace. The rate of temperature increasing was fixed at 20 °C/min. After completing the annealing, the sample naturally cooled down to room temperature (RT). X-ray diffraction (XRD) and electrochemical impedance spectroscopy (EIS) measurements (Fig. S2) suggest the high quality of the prepared Li_6PS_5Cl electrolyte.

2.3. Preparation of the LZO@LCO/LPSCl cathode composite

LZO@LCO powder and LPSCl electrolytes were mixed with a mass ratio of 7:3 using a roll mixer. No conductive carbon was added due to the intrinsic electronic conductive property of the LCO materials. Similar process was employed to prepare ZrO_x@LCO/LPSCl cathode composites.

2.4. Ionic conductivity measurements

According to the previously published method [35], firstly, 1000c ALD-LZO films prepared by 230, 270, and 300 °C respectively were deposited on the glass slides with Au patterns. Then, the ionic conductivity of prepared the ALD-LZO film was measured by the EIS and corresponding simulation method. This was completed on a multichannel potentiostation 3/Z (German VMP3). The applied frequency range is 0.1 Hz–7 MHz and the amplitude is 20 mV. To obtain the Arrhenius plot, variable-temperature EIS was measured from 25 °C to 65 °C with an interval of 10 °C. The ionic conductivity (σ) of our ALD-LZO films was calculated by the equation: $\sigma = d/(R \cdot A)$, where the R is resistance measured by EIS, d and A are the thickness and the area of the deposited ALD-LZO film, respectively.

2.5. Assembly and electrochemical measurements of ASSLIBs

ASSLIBs were fabricated using LPSCl as the electrolyte, LZO@LCO/LPSCl as the cathode composite, and In foil as the anode. Typically, 80 mg of the LPSCl electrolyte was pressed under ~300 MPa to form a solid LPSCl layer (10 mm of diameter). 10 mg of LZO@LCO/LPSCl composite powder were uniformly spread onto the surface of the other side of LPSCl layer and pressed under ~360 MPa for 5 min. Finally, In foil was placed on the other side of the LPSCl pellet and pressed by ~120 MPa for 3 min. The three-layered pellet cell was sandwiched between two stainless-steel rods as current collectors and sealed in the model cell. All cell fabrication processes were performed in an Ar-filled glove box. The loading mass of active material is ~8.92 mg/cm^2 in the ASSLIBs. Galvanostatic charge-discharge was conducted on the LAND battery test system. The voltage window was set as 1.9–3.6 V (vs. In^+/In), and various constant charging/discharging current densities were applied to evaluate the cycling

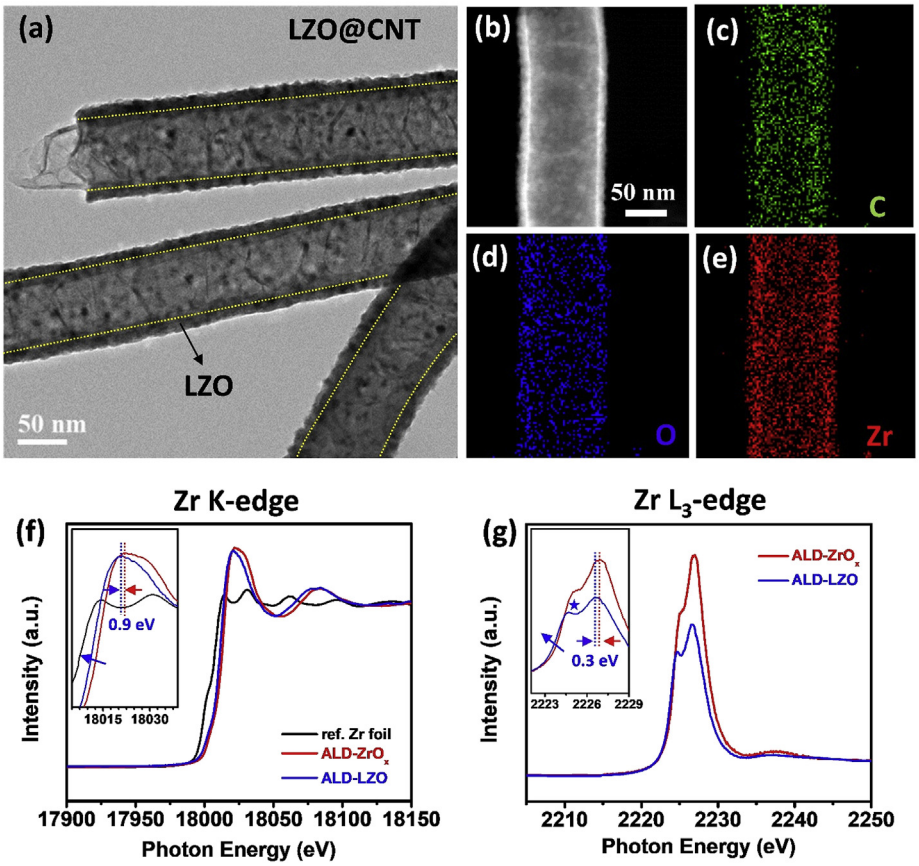

Fig. 1. Characterizations of the prepared ALD-LZO film on CNTs. (a) a TEM image of the deposited LZO films on CNTs (LZO@CNT); (b) a STEM image of the LZO@CNT material; (c–e) EDX mapping of the C, O, and Zr elements on the LZO@CNT; (f and g) comparison of the XANES of Zr K-edge and L_3-edge spectra between the ALD deposited ZrO_x and LZO films.

stability and the rate capability. The galvanostatic intermittent titration technique (GITT) measurements were carried out using LAND battery test station. The transient discharge voltage profiles were recorded by applying a discharge current density of 0.01 C for 5 min followed by a 2h relaxation until the discharge voltage reaches 1.9 V. Cyclic voltammograms (CV) were performed on a VMP3 working station by applying a scan rate of 0.1 mV/s in a voltage range of 1.9–3.6 V. EIS measurements for ASSLIBs at the specific discharge/charge states were completed on the VMP3 station with an amplitude of 20 mV and frequencies ranging from 0.1 H to 7 MHz.

2.6. Characterization methods

X-ray diffraction (XRD) measurements were performed on Bruker AXS D8 Advance with Cu Kα radiation (λ = 1.5406 Å). Scanning electron microscope (SEM) images were obtained by using a Hitachi S-4800 field-emission scanning electron microscope (FE-SEM, acceleration voltage 5 kV). Transmission electron microscope (TEM) images were obtained using a JEOL 2010F field emission TEM (acceleration voltage 200 kV), which is equipped with energy dispersive spectroscopy (EDS) for elemental mapping. X-ray photoelectron spectroscopy (XPS) spectra were obtain by using Krotos AXIS Ultra Spectrometer system using a monochromatic Al K(alpha) source (25 mA, 15 kV). X-ray absorption near edge structure (XANES) spectra of Zr L-edge and K-edge were collected on the Soft X-ray Microcharacterization beamline (SXRMB, 1700–10000 eV) and Hard X-ray MicroAnalysis (HXMA, 5000–40000 eV) beamlines respectively at the Canadian Light Source (CLS). The energy scanning steps for collecting spectra were set as 0.2 eV on SXRMB and 0.5 eV on HXMA, respectively. SXRMB and HXMA data was processed with Athena software. Scanning transmission X-ray microscopy (STXM) was carried out on the Soft X-ray Spectromicroscopy (SM, 130–2700 eV) beamline at CLS. STXM data was analyzed using the aXis2000 software.

3. Results and discussion

3.1. Effects of the introduced Li sub-cycle for obtained ALD-LZO films

The preparation of ALD films follows a layer-by-layer deposition process. Inspired by the previously published ALD processes by our group [35,36], we choose solid-state organic metal-based compounds: TDMAZ and LiO^tBu as the Zr and Li precursors, respectively. H_2O is chosen as the oxidant for the sub-cycles. One single layer (one cycle) of Li containing LZO film can be obtained by alternatively introducing LiO^tBu, H_2O, TDMAZ, and H_2O onto the substrate placed in the ALD chamber. The growth rate of the ALD-LZO film at a chamber temperature of 270 °C is 0.234 nm/cycle, which is determined by measuring the thickness of the deposited ALD-LZO films with various cycles on Si wafers (Fig. S3). 50-cycles (50c) ALD-LZO film are deposited on the carbon nanotube (CNT) substrate (marked as LZO@CNT) for studying the structure of the ALD-LZO film. TEM measurements are carried out to witness an intact LZO coating layer decorates walls of the CNT (Fig. 1a). The elemental mapping under the STEM (scanning transmission electron microscope) mode indicates that C, O, and Zr elements are homogeneously dispersed with spatial resolution in the LZO@CNT composite (Fig. 1b–e). High-energy XPS measurements are used to observe the Li 1s spectrum as shown in Fig. S4a, indicating Li is successfully introduced in the deposited LZO film. The Zr 3d spectrum of LZO film in Fig. S4b shows typical 3d splitting peaks (184.2 and 181.8 eV for $3d_{5/2}$ and $3d_{3/2}$, respectively) of the Zr element, which agrees well with the LZO-related materials

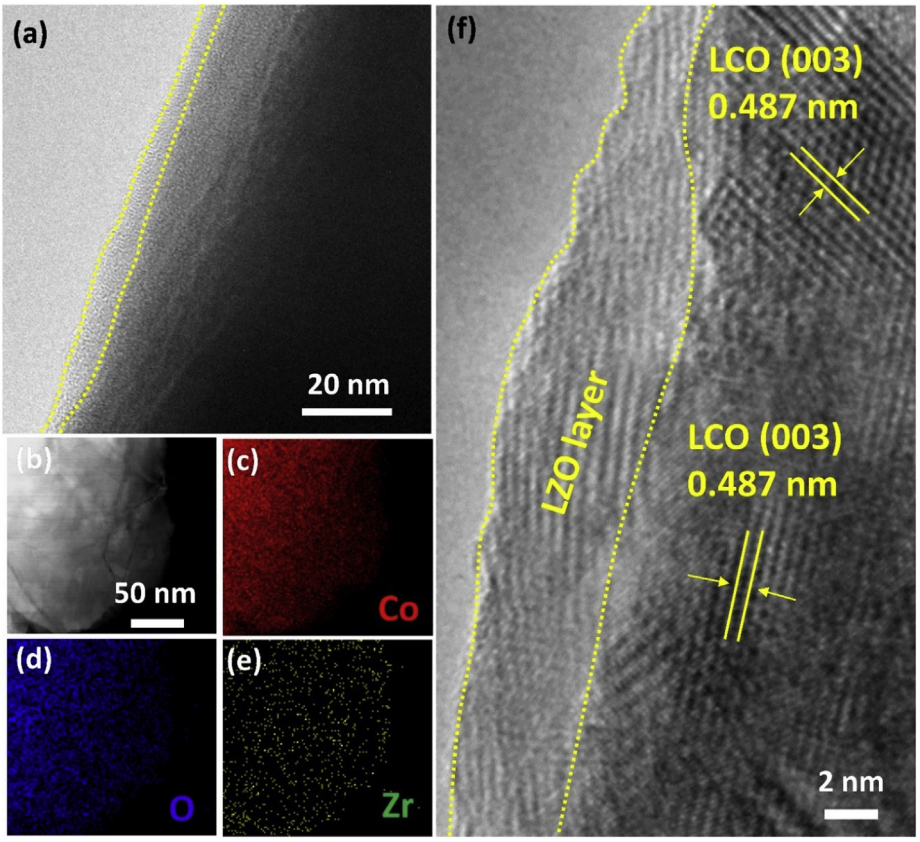

Fig. 2. TEM characterizations of the 25 cycles of ALD-LZO deposited on the LCO particles (LZO@LCO). (a) a TEM image of the LZO@LCO composites; (b) a STEM image of the LZO@LCO composites; (c–e) EDX mapping of the Co, O, and Zr elements on the LZO@LCO composites; (f) a HRTEM image of LZO@LCO composites.

prepared by wet chemical methods [37,38]. XRD measurements cannot witness additional diffraction peaks for the LZO@CNT composites (Fig. S5), indicating the amorphous nature of the deposited LZO films, which agrees well with the previously reported ALD coatings developed at low temperature (<300 °C) [29]. To investigate the influence of introducing Li on the electronic structure of Zr in the ALD films (LZO and ZrO_x), XANES of Zr K-edge and L-edge were collected. Zr K-edge spectra of ALD-LZO and ALD-ZrO_x show distinct spectral features associated with oxidized zirconia species compared to that of the Zr foil reference sample (Fig. 1f). The whiteline peak is seen to undergo a ~0.9 eV shift to a lower energy for the LZO compared with the ZrO_x, suggesting that the incorporated Li can interact with the Zr local environment as previously reported in other Li containing ternary oxides [35,39]. A similar red-shift of photon energy is also reflected in the Zr L_3-edge spectra as shown in Fig. 1g. The intensity of a small broad speak at ~2224.7 eV increases after Li incorporation, indicating electropositive Li^+ slightly lower the chemical state of Zr, and the polymerization degree of Zr–O polyhedrons in the LZO structure is reduced [39]. These morphology and structure characterizations suggest that the simple addition of the sub-cycle with Li incorporating can successfully prepared ALD-LZO film. The distortion of the Zr environment induced by Li incorporation, as well as the disordered Zr–O polyhedron are expected to benefit the Li^+ ion migration in the LZO structure. ALD-LZO films of 1000 cycles are deposited onto the patterned glass slide for the electrochemical impedance spectroscopy (EIS) measurements. Nyquist plots under varied test temperatures and the derived Arrhenius plots are displayed in Fig. S6. The ALD chamber temperature is optimized to be 270 °C for a decent ionic conductivity of 6.7×10^{-5} mS/cm at room temperature (RT) with an activation energy (E_a) of 0.39 eV. The Li^+ transport ability (especially the E_a) of LZO has overtaken other Li containing ternary oxides prepared by ALD methods [40], and can be comparable to the most popular LNO coating for sulfide electrolyte-based ASSLIBs [41].

3.2. ALD-LZO coating on LCO cathode materials

The high-quality ALD-LZO films (deposition temperature at 270 °C, 25c) are deposited on LCO particles (marked as LZO@LCO) to evaluate this functional coating layer in ASSLIBs. First of all, the morphology and structure of LZO@LCO composites are investigated to confirm the core-shell features. The TEM image (Fig. 2a) indicates the thin layer of LZO film with thickness of ~5 nm is continuous and acts as the outermost shell. The spatial distribution of Co, O, and Zr elements in the area of Fig. 2b is revealed by the STEM-elemental mapping (Fig. 2c–e). The signal intensity of Co element in the edge region is obviously weaker than that in the center, while the signal indication of Zr is consistent in the whole area. This illustrates the LZO film is conformally coated on the LCO particle. High-resolution TEM (Fig. 2f) on a local area further verifies the LZO layer is coated on the well crystallized LCO particle. The clear and intact crystal lattice of the (003) plane of internal LCO core confirms that the low temperature deposition temperature (270 °C) has little side effect on the structure of LCO cathode materials. The XPS spectrum of Zr 3d in the LZO@LCO composite is presented in Fig. S7. Splitting positions (184.3 and 181.9 eV for $3d_{5/2}$ and $3d_{3/2}$, respectively) of the Zr 3d spectrum are consistent with that shown in the LZO@CNT composite, suggesting the success of LZO coating on LCO particles. This obtained amorphous LZO coating avoids the formation of island structure of the crystallized coating [27], and benefits to generate an intact protection layer. In addition, the verified high ionic conductivity of this interfacial LZO coating can boost the required electrochemical reactions.

3.3. Excellent electrochemical performance of ASSLIBs

The LZO@LCO cathode composite is combined with Argyrodite Li_6PS_5Cl (LPSCl) sulfide SSEs and In anode to construct full batteries (In//LPSCl//LZO@LCO/LPSCl). The ALD-LZO coating layer is expected

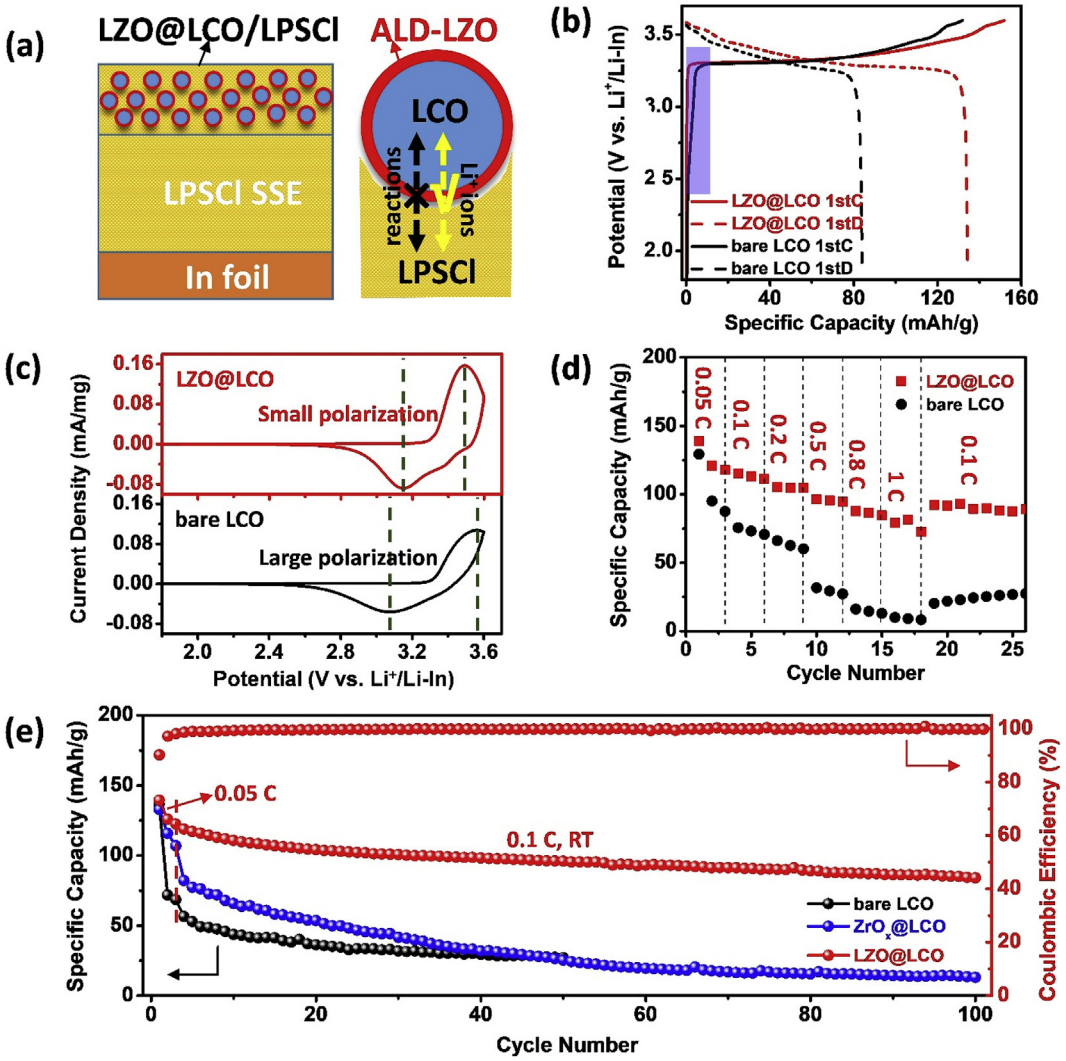

Fig. 3. (a) A schematic diagram of the In//LPSCl//LZO@LCO/LPSCl all-solid-state battery and the proposed mechanism; (b) charge and discharge curves (0.025 C); (c) the first-cycle CV results at a scan rate of 0.1 mV/s; (d) rate capability and (e) long-term cycling stability of all-solid-state batteries with bare LCO, ZrO_x@LCO, and LZO@LCO cathodes. All electrochemical performances were obtained at room temperature (RT).

not only to provide sufficient Li^+ ion flux at the cathode interface, but also to prevent the side reactions, which is illustrated in Fig. 3a. First-cycle charge and discharge curves at a current density of 0.025 C (1 C = 140 mA/g_{LCO}) are displayed in Fig. 3b. In the marked area of the charging curves, a slope exists in the first charging (1stC) curve of the In//LPSCl//LCO/LPSCl full battery without LZO coating, which is attributed to the space charge layer derived from the incompatible interface between oxide cathode materials and sulfide electrolytes [42]. However, this slope vanishes for the In//LPSCl//LZO@LCO/LPSCl full battery with LZO coating, which means the LZO coating layer can flatten the charge distribution and promote a stable LCO/LPSCl interface. As a result, the specific capacity of LCO cathode materials after coating LZO is 134.3 mAh/g with a high first-cycle coulombic efficiency of 89.0%. By contrast, the LCO cathode without LZO coating just exhibits a reversible specific capacity of 84.1 mAh/g and a much lower first-cycle coulombic efficiency of 63.8%. Cyclic voltammetry (CV) measurements verify that a large polarization occurs in the positive (charging) and negative (discharging) scan if LZO protection layer is not coated on the LCO cathode (Fig. 3c). The rate capability of the In//LPSCl//LZO@LCO/LPSCl full battery is studied in detail. As displayed in Fig. 3d, the reversible specific capacity at 0.05 C is 121.8 mAh/g, and gradually declines to 115.4, 104.6, 95.6, and 87.8 mAh/g when the current density increases to 0.1, 0.2, 0.5, and 0.8 C, respectively. Even at a high current density of 1 C, the specific capacity of 79.1 mAh/g can be retained. Importantly, the specific capacity is able to recover to 92.3 mAh/g when the current density reduces to 0.1 C. In sharp contrast, the bare LCO cathode exhibits poor lithiation kinetics when the current density elevates to 0.5 C, because very limited reversible capacity (~25 mAh/g) is obtained at this current. The rate capability based on ALD-LZO coating has overtaken that performed with the most popular LNO coating [31]. We ascribe this enhancement to the good electrical band structure derived by the Zr-containing interface [18]. Long-term cycling stability of the In//LPSCl//LZO@LCO/LPSCl full battery is reflected in Fig. 3e. After the initial three charging and discharging cycles at low current density of 0.05 C, the charged specific capacity of the full battery reaches 117.2 mAh/g at a current density of 0.1 C, and maintains 84.1 mAh/g (72% retention) after 100 cycles. Without LZO coating, the initial reversible capacity is 56.7 mAh/g, and drop to only 27.2 mAh/g at the 50th cycle. Obviously, the good performance via LZO coating layers cannot be achieved equivalently with ALD-ZrO_x coating (100c). The poor cycling stability and limited reversible specific capacity of ZrO_x@LCO cathode demonstrate the significance of introducing Li in the coating layer. The Li containing coating layer cannot only prevent the side reactions, but also provide essential support for the Li^+ ion migration at the interface of cathode/sulfide SSEs. In addition, we coated LCO particles with different layer numbers of LZO films to optimize the thickness of the ALD-LZO

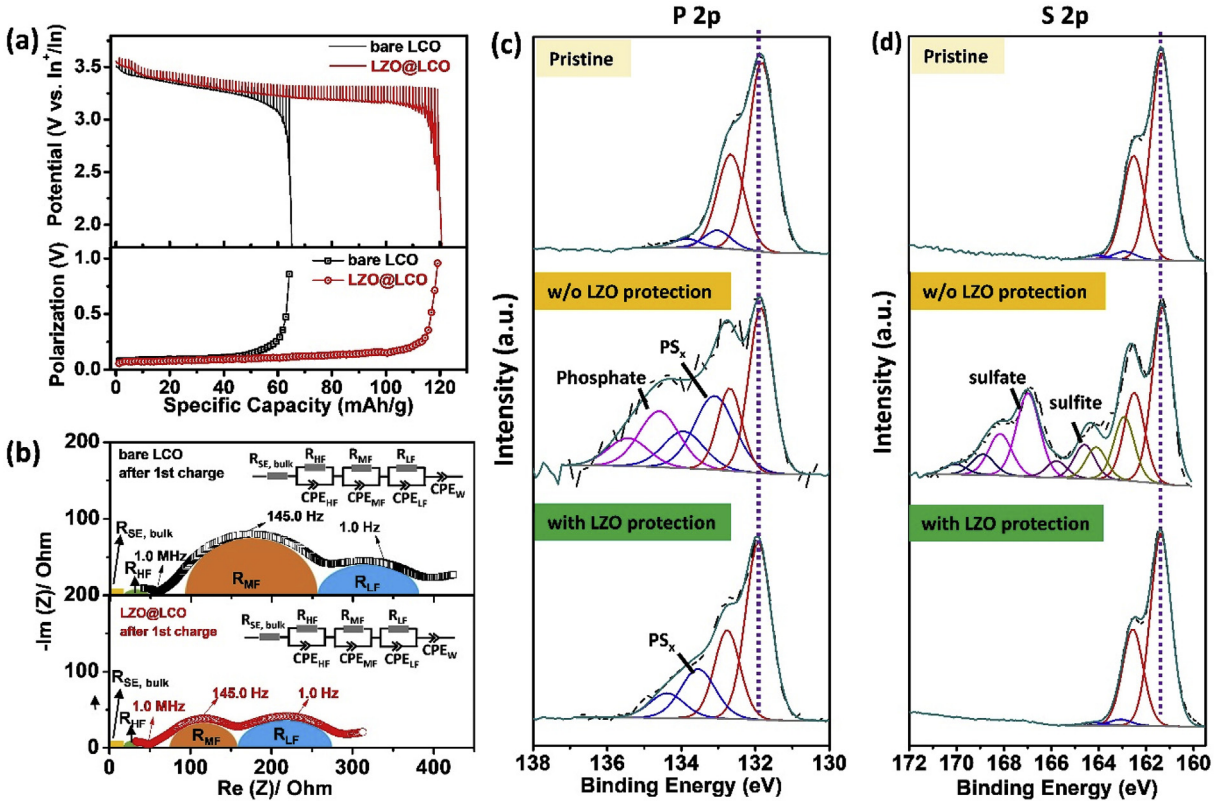

Fig. 4. (a) Comparisons of the transient discharge voltage profiles and their corresponding polarization plots obtained by GITT, and (b) EIS analysis results for In//LPSCl//LZO@LCO/LPSCl and In//LPSCl//LCO/LPSCl full batteries; (c and d) XPS spectra of the P 2p and S 2p before and after battery cycling with and w/o LZO protections on the LCO cathode particles.

protection layer. Compared with 10c and 50c LZO coating layers, 25c LZO exhibits the optimal thickness (~5 nm) which shows the best cycling stability in In//LPSCl//LZO@LCO/LPSCl full batteries (Fig. S8). A thinner LZO coating layer (Fig. S9a) cannot ensure an intact protection layer on the LCO particle, while too thick of a LZO coating layers (Fig. S9c) would hinder the Li^+ ion transfer through the interface. It is noted that the cycling stability of our ASSLIBs with the protection of ALD-LZO coating on LCO cathode has also surpassed previously reported result with LNO coating [31,43,44]. We further correlate the effect of the interfacial ionic conductivity to the battery performance by examining the LZO film deposited on LCO cathodes at 230 °C and 300 °C. The result suggests that LZO obtained via 230 °C with lower ionic conductivity compared with those gained at 270 °C or 300 °C, delivering a lower specific capacity, faster capacity decay rate, as well as lower coulombic efficiency (Fig. S10). In addition, the LZO film obtained at 300 °C on LCO particles is inferior to that obtained via 270 °C. This is ascribed to the larger growth rate of the LZO layer at higher deposition temperature. The resulting thicker LZO layer (Fig. S11) is undesirable for the effective Li^+ ion transport at the interface between LCO cathodes and LPSCl SSEs.

3.4. Understanding the mechanism of the ALD-LZO derived cathode interface

Various electrochemical and chemical structure characterizations were utilized to understand the functional mechanism of ALD-LZO coating layers on LCO cathode. Galvanostatic intermittent titration technique (GITT) was employed to track the polarization of full batteries. Transient discharging voltage profiles and the derived polarization curves are displayed in Fig. 4a. In the spontaneous discharging process, LZO@LCO cathode shows lower polarization than bare LCO. Especially after delivering a specific capacity of 50 mAh/g, the LZO coating layer can significantly prolong the discharge process of LCO cathode with a much smaller polarization. This means ALD-LZO induces a favorable interface between LCO cathode and LPSCl electrolytes, which can effectively reduce the interfacial polarization. EIS measurements were performed for the full batteries after the first charging process. Fig. 4b shows the Nyquist plots with the corresponding equivalent circuits. The similar R_{SE} value (~22 Ω) imply a similar bulk resistance of the LPSCl layer in the two full batteries using bare LCO and LZO@LCO based cathode materials [45]. The LPSCl/In anode interface impedance can be described as R_{LF} (low-frequency region). A similar R_{LF} value (~120 Ω) helps to rule out any anode influence when analyzing the cathode part. The semi-circles at the middle-frequency and high-frequency represent the impedances of cathode composite layer/LPSCl layer interface (R_{MF}) and cathode materials/LPSCl interface in the cathode composite (R_{HF}), respectively [45–47]. After coating LCO with ALD-LZO films, these two values reduce significantly upon battery cycling, which is related to the inhibition of side reactions and fast Li^+ ions mobility at the advanced cathode/LPSCl interface with LZO coating.

XPS analysis were conducted on the cycled cathode composite with and without (w/o) LZO protection. P 2p and S 2p spectra present in Fig. 4c and d, respectively. P in the LPSCl can be oxidized to phosphorus polysulfides (PS_x) and phosphate upon electrochemically reacting with bare LCO cathode materials [48,49]. Similarly, S is oxidized to high-valence sulfites and sulfates without LZO protection [49,50]. These findings are in accordance with previously reported results, which are due to the incompatibility of the sulfide/LCO interface and the instability of LPSCl SSEs at voltages higher than 2.8 V [48–50]. In contrast, the electrochemically instable LCO/LPSCl interface can be alleviated by coating LCO with ALD-LZO. Although some PS_x species resulting from the decomposition of LPSCl at high voltage still exists in the cathode composite (with LZO protection) after cycling, the detrimental side reactions is prevented significantly and the S spectrum is maintained well. In addition, the XPS of Zr 3d spectrum (Fig. S12) in the cycled cathode

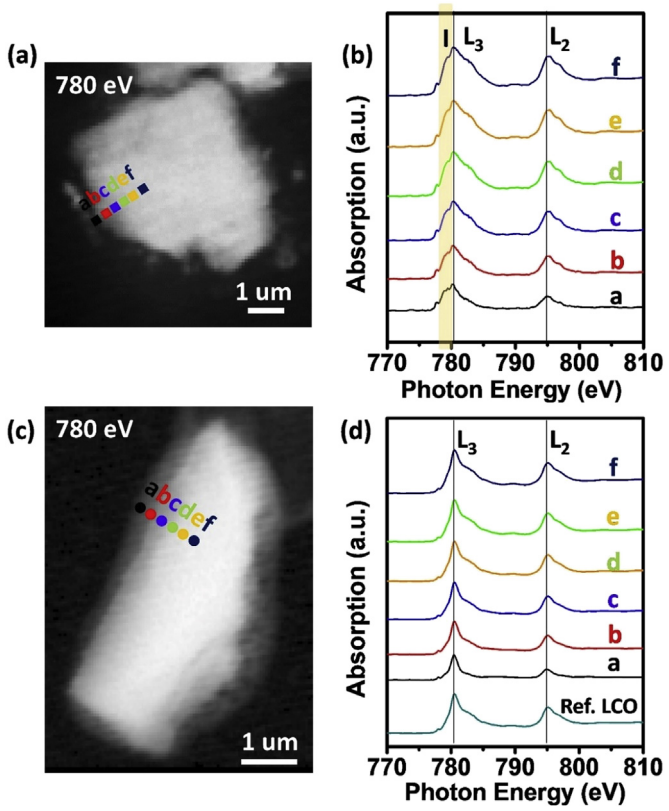

Fig. 5. STXM optical density images of single LCO particle after 50 cycles of charging and discharging with bare LCO cathode (a) and LZO@LCO cathode (c), respectively. (b) XANES of Co $L_{3,2}$ edge of the marked areas in (a). (d) XANES of Co $L_{3,2}$ edge of the marked areas in (c).

composite remains unchanged, indicating the ALD-LZO coating layer is robust and can withstand repeat Li^+ ion transfer through the LZO@LCO/LPSCl interface. Due to the limited emission energy of XPS, no difference can be observed on the Co 2p spectra of the cycled LCO cathode with or without LZO coating (Fig. S13). However, we can observe two kinds of distinct spectra of Co L-edge through synchrotron-based STXM. On the absorption edge (780 eV), micro-sized single LCO particles without and with LZO coating can be imaged as shown in Fig. 5a and Fig. 5c, respectively. The spectra of Co $L_{3,2}$ edge (Fig. 5b) extracted from the marked areas in Fig. 5a show that a broad peak (peak I) always exists, indicating the Co^{3+} in the LCO cathode was reduced when in contact with LPSCl directly after cycling [51,52]. The reduction reaction of Co^{3+} can be eliminated by the LZO protection. As shown in Fig. 5d, the spectra corresponding to the marked positions remain consistent compared with the spectrum of Co $L_{3,2}$ edge in pristine LCO.

4. Conclusion

In summary, ALD is utilized to rationally design Li-containing Zr-based cathode coating for sulfide-based ASSLIBs. Structural characterizations (including synchrotron-XANES) confirm the success of incorporating Li in the LZO film by an additional Li-related sub-cycle process, which affects the local electronic structure of the Zr metal centers. The presented Zr–Li interaction manipulated by the ALD deposition temperature (270 °C) is demonstrated to be favorable for a desirable ionic conductivity of 6.7×10^{-5} mS/cm at room temperature. ALD-LZO films coated on LCO cathode materials can significantly improve the RT performance for full batteries. A specific capacity of 117.2 mAh/g is achieved at the current density of 0.1 C, and the capacity retention stands at 72% after 100 cycles. More importantly, the specific capacity reaches 79.1 mAh/g at 1 C. The effective interfacial manipulation provides essential Li^+ ion flux at the LCO/LPSCl interface, which can reduce the polarization of the electrochemical reactions. Moreover, various spectroscopic characterizations (XPS and synchrotron-STXM) reveal that the detrimental side reactions between LCO and LPSCl are significantly reduced with the LZO derived cathode interface. The flexible design of functional cathode interface realized by ALD paves the way to achieve advanced sulfide-based ASSLIBs.

CRediT authorship contribution statement

Feipeng Zhao: Conceptualization, Investigation, Methodology, Data curation, Formal analysis, Writing - original draft. **Yang Zhao:** Methodology, Data curation, Formal analysis, Writing - review & editing. **Jian Wang:** Methodology, Data curation, Formal analysis, Writing - review & editing. **Qian Sun:** Data curation, Formal analysis. **Keegan Adair:** Formal analysis, Writing - review & editing. **Shumin Zhang:** Formal analysis, Writing - review & editing. **Jing Luo:** Formal analysis, Writing - review & editing. **Junjie Li:** Data curation, Formal analysis. **Weihan Li:** Data curation, Formal analysis. **Yipeng Sun:** Data curation, Formal analysis. **Xiaona Li:** Formal analysis. **Jianwen Liang:** Formal analysis, Writing - review & editing. **Changhong Wang:** Writing - review & editing. **Ruying Li:** Resources. **Huan Huang:** Funding acquisition. **Li Zhang:** Funding acquisition, Writing - review & editing. **Shangqian Zhao:** Funding acquisition, Writing - review & editing. **Shigang Lu:** Funding acquisition, Project administration. **Xueliang Sun:** Writing - review & editing, Funding acquisition, Project administration, Supervision, Conceptualization.

Declaration of competing interest

The authors declare that they have no known competing financial interests or personal relationships that could have appeared to influence the work reported in this paper.

Acknowledgements

This research was supported by the Natural Sciences and Engineering Research Council of Canada (NSERC), the Canada Research Chair Program (CRC), the Canada Foundation for Innovation (CFI), Ontario Research Foundation (ORF), China Automotive Battery Research Institute Co., Ltd., Glabat Solid-State Battery Inc. and Western University. The synchrotron research described in this work was performed at the Canadian Light Source, which is supported by the Canada Foundation for Innovation (CFI), the Natural Sciences and Engineering Research Council (NSERC), the Canadian Institutes of Health Research (CIHR), and the Government of Saskatchewan. We also appreciate the help of the beamline scientists of SXRMB and HXMA beamlines at Canadian Light Source, Dr. Yonfeng Hu, Dr. Qunfeng Xiao, Dr. Mohsen Shakouri, Dr. Ning Chen, and Dr. Weifeng Chen.

Appendix A. Supplementary data

Supplementary data to this article can be found online at https://doi.org/10.1016/j.ensm.2020.06.013.

References

[1] Y. Kato, S. Hori, T. Saito, K. Suzuki, M. Hirayama, A. Mitsui, M. Yonemura, H. Iba, R. Kanno, Nat. Energy 1 (2016), 16030.
[2] A. Manthiram, X. Yu, S. Wang, Nat. Rev. Mater. 2 (2017), 16103.
[3] Y. Ding, Z.P. Cano, A. Yu, J. Lu, Z. Chen, Electrochem. Energy Rev. 2 (2019) 1–28.
[4] Y. Xiao, Y. Wang, S.-H. Bo, J.C. Kim, L.J. Miara, G. Ceder, Nat. Rev. Mater. 5 (2020) 105–126.
[5] Q. Zhang, D. Cao, Y. Ma, A. Natan, P. Aurora, H. Zhu, Adv. Mater. 31 (2019), 1901131.
[6] F. Zhao, J. Liang, C. Yu, Q. Sun, X. Li, K. Adair, C. Wang, Y. Zhao, S. Zhang, W. Li, S. Deng, R. Li, Y. Huang, H. Huang, L. Zhang, S. Zhao, S. Lu, X. Sun, Adv. Energy Mater. 10 (2020), 1903422.

[7] R. Kanno, M. Murayama, T. Inada, T. Kobayashi, K. Sakamoto, N. Sonoyama, A. Yamada, S. Kondo, Electrochem. Solid State Lett. 7 (2004) A455–A458.
[8] X.N. Li, J.W. Liang, X. Li, C.H. Wang, J. Luo, R.Y. Li, X.L. Sun, Energy Environ. Sci. 11 (2018) 2828–2832.
[9] K. Takada, N. Aotani, K. Iwamoto, S. Kondo, Solid State Ionics 86–88 (1996) 877–882.
[10] Y.H. Xiao, L.J. Miara, Y. Wang, G. Ceder, Joule 3 (2019) 1252–1275.
[11] R. Chen, Q. Li, X. Yu, L. Chen, H. Li, Chem. Rev. (2019), https://doi.org/10.1021/acs.chemrev.1029b00268.
[12] C.H. Wang, K.R. Adair, J.W. Liang, X.N. Li, Y.P. Sun, X. Li, J.W. Wang, Q. Sun, F.P. Zhao, X.T. Lin, R.Y. Li, H. Huang, L. Zhang, R. Yang, S.G. Lu, X.L. Sun, Adv. Funct. Mater. 29 (2019), 1900392.
[13] S.P. Culver, R. Koerver, W.G. Zeier, J. Janek, Adv. Energy Mater. 9 (2019), 1900626.
[14] M. Du, K. Liao, Q. Lu, Z. Shao, Energy Environ. Sci. 12 (2019) 1780–1804.
[15] S. Ito, S. Fujiki, T. Yamada, Y. Aihara, Y. Park, T.Y. Kim, S.W. Baek, J.M. Lee, S. Doo, N. Machida, J. Power Sources 248 (2014) 943–950.
[16] Y.G. Lee, S. Fujiki, C. Jung, N. Suzuki, N. Yashiro, R. Omoda, D.S. Ko, T. Shiratsuchi, T. Sugimoto, S. Ryu, J.H. Ku, T. Watanabe, Y. Park, Y. Aihara, D. Im, I.T. Han, Nat. Energy 5 (2020) 299–308.
[17] N. Machida, J. Kashiwagi, M. Naito, T. Shigematsu, Solid State Ionics 225 (2012) 354–358.
[18] X.F. Li, J. Liu, X.B. Meng, Y.J. Tang, M.N. Banis, J.L. Yang, Y.H. Hu, R.Y. Li, M. Cai, X.L. Sun, J. Power Sources 247 (2014) 57–69.
[19] X. Li, K.J. Zhang, D. Mitlin, Z.Z. Yang, M.S. Wang, Y. Tang, F. Jiang, Y.G. Du, J.M. Zheng, Chem. Mater. 30 (2018) 2566–2573.
[20] Israel science and technology directory. https://www.science.co.il/elements/?s=Earth.
[21] J.C. Zhang, Z.Y. Li, R. Gao, Z.B. Hu, X.F. Liu, J. Phys. Chem. C 119 (2015) 20350–20356.
[22] J. Ni, H. Zhou, J. Chen, X. Zhang, Electrochim. Acta 53 (2008) 3075–3083.
[23] B. Song, W. Li, S.M. Oh, A. Manthiram, ACS Appl. Mater. Interfaces 9 (2017) 9718–9725.
[24] J.C. Zheng, Z. Yang, P.B. Wang, L.B. Tang, C.S. An, Z.J. He, ACS Appl. Mater. Interfaces 10 (2018) 31324–31329.
[25] J.C. Zhang, H. Zhang, R. Gao, Z.Y. Li, Z.B. Hu, X.F. Liu, Phys. Chem. Chem. Phys. 18 (2016) 13322–13331.
[26] C. Wang, L. Chen, H. Zhang, Y. Yang, F. Wang, F. Yin, G. Yang, Electrochim. Acta 119 (2014) 236–242.
[27] Y.J. Lim, S.M. Lee, H. Lim, B. Moon, K.S. Han, J.H. Kim, J.H. Song, J.S. Yu, W. Cho, M.S. Park, Electrochim. Acta 282 (2018) 311–316.
[28] S.M. George, Chem. Rev. 110 (2010) 111–131.
[29] Y. Zhao, K. Zheng, X.L. Sun, Joule 2 (2018) 2583–2604.
[30] X. Li, Z.H. Ren, M.N. Banis, S.X. Deng, Y. Zhao, Q. Sun, C.H. Wang, X.F. Yang, W.H. Li, J.W. Liang, X.N. Li, Y.P. Sun, K. Adair, R.Y. Li, Y.F. Hu, T.K. Sham, H. Huang, L. Zhang, S.G. Lu, J. Luo, X.L. Sun, ACS Energy Lett 4 (2019) 2480–2488.
[31] C.H. Wang, X. Li, Y. Zhao, M.N. Banis, J.W. Liang, X.N. Li, Y.P. Sun, K.R. Adair, Q. Sun, Y.L. Liu, F.P. Zhao, S.X. Deng, X.T. Lin, R.Y. Li, Y.F. Hu, T.K. Sham, H. Huang, L. Zhang, R. Yang, S.G. Lu, X.L. Sun, Small Methods 3 (2019), 1900261.
[32] S. Deng, X. Li, Z. Ren, W. Li, J. Luo, J. Liang, J. Liang, M.N. Banis, M. Li, Y. Zhao, X. Li, C. Wang, Y. Sun, Q. Sun, R. Li, Y. Hu, H. Huang, L. Zhang, S. Lu, J. Luo, X. Sun, Energy Storage Mater 27 (2020) 117–123.
[33] H. Yadegari, M.N. Banis, B.W. Xiao, Q. Sun, X. Li, A. Lushington, B.Q. Wang, R.Y. Li, T.K. Sham, X.Y. Cui, X.L. Sun, Chem. Mater. 27 (2015) 3040–3047.
[34] C. Yu, Y. Li, M. Willans, Y. Zhao, K.R. Adair, F.P. Zhao, W.H. Li, S.X. Deng, J.W. Liang, M.N. Banis, R.Y. Li, H. Huang, L. Zhang, R. Yang, S.G. Lu, Y.N. Huang, X.L. Sun, Nano Energy 69 (2020) 104396.
[35] B. Wang, Y. Zhao, M.N. Banis, Q. Sun, K.R. Adair, R. Li, T.K. Sham, X. Sun, ACS Appl. Mater. Interfaces 10 (2018) 1654–1661.
[36] J. Liu, X. Meng, M.N. Banis, M. Cai, R. Li, X. Sun, J. Phys. Chem. C 116 (2012) 14656–14664.
[37] W.L. Wang, Z.L. Yin, J.P. Wang, Z.X. Wang, X.H. Li, H.J. Guo, J. Alloys Compd. 651 (2015) 737–743.
[38] D. Wang, X.H. Li, Z.X. Wang, H.J. Guo, Z.J. Huang, L.K. Kong, J.J. Ru, J. Alloys Compd. 647 (2015) 612–619.
[39] B. Wang, J. Liu, M. Norouzi Banis, Q. Sun, Y. Zhao, R. Li, T.K. Sham, X. Sun, ACS Appl. Mater. Interfaces 9 (2017) 31786–31793.
[40] E. Kazyak, K.-H. Chen, A.L. Davis, S. Yu, A.J. Sanchez, J. Lasso, A.R. Bielinski, T. Thompson, J. Sakamoto, D.J. Siegel, N.P. Dasgupta, J. Mater. Chem. 6 (2018) 19425–19437.
[41] A.M. Glass, K. Nassau, T.J. Negran, J. Appl. Phys. 49 (1978) 4808–4811.
[42] J. Haruyama, K. Sodeyama, L.Y. Han, K. Takada, Y. Tateyama, Chem. Mater. 26 (2014) 4248–4255.
[43] N. Ohta, K. Takada, I. Sakaguchi, L.Q. Zhang, R.Z. Ma, K. Fukuda, M. Osada, T. Sasaki, Electrochem. Commun. 9 (2007) 1486–1490.
[44] N. Kamaya, K. Homma, Y. Yamakawa, M. Hirayama, R. Kanno, M. Yonemura, T. Kamiyama, Y. Kato, S. Hama, K. Kawamoto, A. Mitsui, Nat. Mater. 10 (2011) 682–686.
[45] N. Ohta, K. Takada, L.Q. Zhang, R.Z. Ma, M. Osada, T. Sasaki, Adv. Mater. 18 (2006) 2226–2229.
[46] A.Y. Kim, F. Strauss, T. Bartsch, J.H. Teo, T. Hatsukade, A. Mazilkin, J. Janek, P. Hartmann, T. Brezesinski, Chem. Mater. 31 (2019) 9664–9672.
[47] K. Okada, N. Machida, M. Naito, T. Shigematsu, S. Ito, S. Fujiki, M. Nakano, Y. Aihara, Solid State Ionics 255 (2014) 120–127.
[48] J. Auvergniot, A. Cassel, J.B. Ledeuil, V. Viallet, V. Seznec, R. Dedryvere, Chem. Mater. 29 (2017) 3883–3890.
[49] A. Banerjee, H.M. Tang, X.F. Wang, J.H. Cheng, H. Nguyen, M.H. Zhang, D.H.S. Tang, T.A. Wynn, E.A. Wu, J.M. Doux, T.P. Wu, L. Ma, G.E. Sterbinsky, M.S. D'Souza, S.P. Ong, Y.S. Meng, ACS Appl. Mater. Interfaces 11 (2019) 43138–43145.
[50] J. Auvergniot, A. Cassel, D. Foix, V. Viallet, V. Seznec, R. Dedryvere, Solid State Ionics 300 (2017) 78–85.
[51] H. Ishii, K. Nakanishi, I. Watanabe, T. Ohta, K. Kojima, e-J. Surf. Sci. Nanotechnol. 9 (2011) 416–421.
[52] Z.Y. Wang, J.Z. Lee, H.L.L. Xin, L.L. Han, N. Grillon, D. Guy-Bouyssou, E. Bouyssou, M. Proust, Y.S. Meng, J. Power Sources 324 (2016) 342–348.